Polskie Towarzystwo Materiałów Kompozytowych
Polish Society of Composite Materials

26: 3 (2026) 192–208

COMPOSITES THEORY AND PRACTICE

ISSN (online): 2299-128X

Zuzanna Pacholec (0009-0002-4384-0344), Karolina Paczkowska* (0009-0007-4170-3406), Jakub Stolarczyk (0009-0003-9570-2506), Marcin Bogucki (0009-0004-5893-9018), Michał Barcikowski (0000-0001-5135-7892), Wojciech Błażejewski (0000-0001-9260-1388), Paweł Bury (0000-0002-1480-0653), Krzysztof Towarnicki (0000-0002-4881-2548), Paweł Stabla* (0000-0001-6891-582X)

Wroclaw University of Science and Technology, 50–371, Wroclaw, Poland
* *Correspondence*: karolina.paczkowska@pwr.edu.pl, pawel.stabla@pwr.edu.pl

Received (Otrzymano) 1.07.2026
Published on-line (Opublikowano) 30.09.2026

FRACTURE TOUGHNESS EVALUATION OF FILAMENT-WOUND CARBON FIBER LAMINATES: CASE STUDY

https://doi.org/10.62753/ctp.2026.04.3.3

Filament-wound fiber-reinforced polymer (FRP) composites are widely used in pressure vessels and tubular structures; however, their interlaminar fracture behavior remains insufficiently understood. This study investigates the fracture toughness of helically wound carbon fiber-reinforced polymer (CFRP) laminates under mode I, mode II, and mixed-mode loading using DCB, ENF, and MMB tests. The results showed that the fracture behavior was strongly influenced by the fiber orientation, fiber cross-over regions, and void content in the composite structure. Fiber interlacing increased the resistance to crack propagation by forcing the crack front to follow a more complex path, while an increased void content reduced the local fracture resistance and promoted crack growth. The mixed-mode tests indicated that the fracture resistance grew with the contribution of mode I loading. The findings demonstrate that the wound laminate structure plays a key role in delamination development and should be considered in the design of filament-wound composite structures.

Keywords: filament winding, interlaminar fracture toughness, delamination, carbon fiber-reinforced polymer (CFRP), mixed-mode fracture

INTRODUCTION

Fiber-reinforced polymer (FRP) composites have become key structural materials due to their high specific stiffness and strength, corrosion resistance, and the possibility of tailoring mechanical performance through fiber orientation and manufacturing technology. They are increasingly used in load-bearing components of transport systems [1, 2, 3], including pressure vessels [4, 5], pipelines [6, 7], drive shafts, structural shells, and lightweight elements in automotive [8, 9, 10], railway, marine, and aerospace [11] applications.

Among the available manufacturing techniques, filament winding is particularly attractive, as it enables the highly automated production of axisymmetric and quasi-axisymmetric structures with controlled fiber placement [5, 7, 12]. Components manufactured using this process are typically subjected to complex service loading conditions combining axial, hoop, torsional, and bending loads [13, 14]. As a result, their structural integrity depends not only on in-plane properties but also on the resistance to interlaminar damage. De-

 All rights reserved

fects leading to premature delamination may originate from manufacturing imperfections, such as microcracks or voids, as well as from in-service damage, which is particularly critical in transport applications [15, 16, 17].

Interlaminar fracture toughness is commonly evaluated using standardized methods such as the double cantilever beam (DCB), end-notched flexure (ENF), and mixed-mode bending (MMB) tests. These methods were originally developed for unidirectional laminates and rely on assumptions of uniform and well-defined fiber alignment. Although they have been widely extended to multidirectional composites [18, 19, 20, 21, 22], including bidirectional and quasi-isotropic laminates, most existing studies focus on materials manufactured from woven fabrics. In such systems, the fiber structure is characterized by periodic interlacing patterns that differ fundamentally from the continuous fiber paths typical of filament-wound structures.

Several studies have highlighted the complexity of interlaminar fracture behavior in multidirectional composite laminates. De Morais [23] demonstrated that mode I fracture toughness values obtained from multidirectional laminates may differ significantly from those measured for unidirectional systems due to residual stresses and local mode-mixity effects. Similarly, Zhao et al. [24] proposed Paris-type models describing fatigue delamination growth in multidirectional CFRP laminates under different mode-mixity ratios, showing that the crack propagation behavior strongly depends on the definition of the strain energy release rate range. Experimental investigations by Wilk [25] introduced alternative procedures for mode I and mode II fatigue delamination testing based on compliance calibration, enabling reliable crack growth characterization without direct visual monitoring of the crack front. Furthermore, Vallmajó [26] reported that ply misalignment can significantly reduce the notched strength of carbon fiber-reinforced laminates, emphasizing the importance of accounting for local variations in fiber orientation and manufacturing-induced imperfections.

Consequently, the damage mechanisms and crack propagation behavior observed in woven or unidirectional laminates may not be fully representative of filament-wound components. In particular, the structural response of wound materials is governed by the winding process, which introduces spatial variability in the fiber orientation, compaction, and thickness. For this reason, the use of conventional flat laminates as representative test specimens for filament-wound structures is of limited relevance. Instead, specimens manufactured by means of the filament winding process provide a more realistic representation of the material structure and its associated fracture behavior.

Despite the increasing industrial application of filament-wound composites, especially in pressure vessels and tubular structures, their interlaminar fracture behavior under different loading modes remains insufficiently investigated. Therefore, further studies are required to assess the applicability of standardized fracture toughness testing methods to filament-wound specimens. In this context, the present work provides an experimental evaluation of fracture behavior in filament-wound carbon-reinforced polymer composites under mode I, mode II, and mixed-mode loading conditions. Owing to the complexity of the material structure, the study is intended as a case-oriented investigation rather than a comprehensive parametric analysis.

MATERIALS AND METHODS

Filament winding process

The rectangular plate from which the specimens were cut was manufactured using a Mikrosam MAW 20 LS4/1 quadriaxial filament winder, with Torayca T700SC/12k (Toray, Japan) carbon fiber and an epoxy resin system consisting of Araldite LY 1564 epoxy resin and Aradur 3486 hardener (both from Huntsman, USA; mixing ratio 100:36 by weight).

The plate was manufactured with a winding angle of ±45°. To prevent fiber slippage at the turnaround zone, pin strips were attached to the sides of the plate. Additionally, rounded-edge inserts were used on the sides where the fibers were redirected to avoid sharp bending (Figure 1).

 All rights reserved

The manufacturing process involved first winding a ±45° layer, followed by the application of a pre-implanted oriented polystyrene insert with a thickness of 100 µm along the edge of the laminate (Figure 2). The insert served as a delamination initiator. Subsequently, a second ±45° layer was wound on top.

Fig. 1. Rectangular plate prepared for filament winding

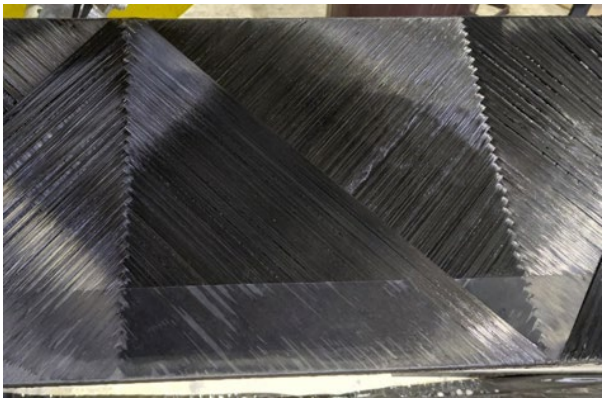

Fig. 2. First layer of composite with insert at bottom edge

Fracture toughness testing

The interlaminar fracture toughness of the specimens was evaluated under mode I, mode II, and mixed-mode I/II loading conditions. The mode I tests were carried out in accordance with ASTM D5528/D5528M-21 using the DCB configuration. The mode II tests were performed following ASTM D7905/D7905M-19, employing the ENF method. The mixed-mode I/II behavior was assessed utilizing the MMB test in accordance with ASTM D6671/D6671M-22. All the experiments were conducted by means of a 2 kN Instron 5944 universal testing machine. Within the framework of fracture mechanics, three fundamental loading modes can be distinguished, and in this study, two of them are considered.

Mode I

Mode I loading is characterized by a tensile force applied perpendicular to the crack plane, resulting in crack propagation driven by opening (tensile) stresses (Figure 3).

In this study, mode I was performed on DCB specimens. This method involves initiating crack propagation with a pre-inserted non-adhesive insert under tensile opening conditions, promoting stable delamination growth along the laminate interface. The applied load generates controlled separation of the adherends, allowing the crack to propagate in a predominantly mode I manner.

During the test, the force–displacement response is continuously recorded, together with the corresponding crack length. These measurements enable evaluation of the interlaminar fracture toughness based on established data reduction methods, providing a quantitative description of the energy required for delamination initiation and propagation [22].

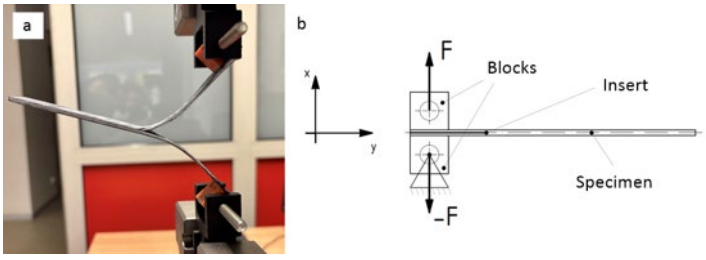

Fig. 3. Mode I testing a) specimen at end of test b) DBC method diagram

Mode II

Mode II is realized through three-point bending, which induces interlaminar shear stresses resulting from the relative sliding of adjacent layers. As a result, the specimen is subjected predominantly to shear at the crack interface (Figure 4). In laminated materials, this loading configuration is particularly critical since it promotes interlayer

displacement and facilitates delamination growth [27, 28].

The ENF test setup is used to evaluate the interlaminar fracture resistance of composite materials under mode II (shear) loading conditions. The specimen, containing a mid-plane pre-crack introduced by a non-adhesive insert, is subjected to three-point bending, resulting in predominantly shear-driven crack propagation along the laminate interface.

The force–displacement response is recorded throughout the experiment, and its analysis enables the material's resistance to crack propagation under shear loading to be determined, typically expressed in terms of the critical energy release rate or maximum load capacity [29].

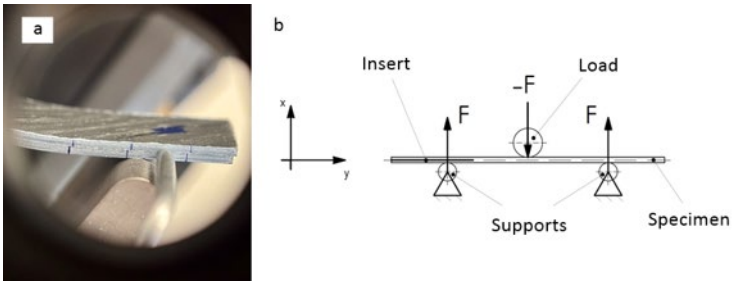

Fig. 4. Mode II a) layer displacement at end of test b) ENF method diagram

Mixed-mode I/II bending

Mixed-mode bending (MMB) combines mode I (opening) and mode II (shear) loading, enabling controlled adjustment of the fracture mode mixity and determination of the total fracture energy (G_c) as well as its mode I (G_I) and mode II (G_{II}) components. The initial crack is defined by a pre-inserted non-adhesive layer.

The mode mixity is governed by the fixture geometry, which determines the relative contribution of opening and shear during crack propagation. The specimen is loaded using a lever-based fixture mounted on a universal testing machine, where the applied force generates simultaneous bending-induced opening and interlaminar shear at the crack tip, Figure 5.

The mode I/mode II ratio is defined before testing by the distance between the loading point and the rotational axis of the fixture, which directly controls the loading configuration during the experiment [30].

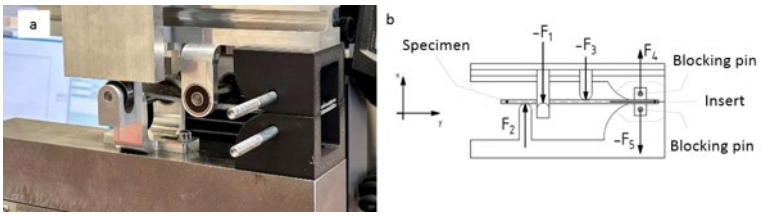

Figure 5. MMB specimen loading conditions

Specimen preparation

Each test configuration was performed on five specimens. The specimen dimensions were 3 × 25 × 150 mm for the DCB and MMB tests, and 3 × 25 × 180 mm for the ENF tests.

DCB

The DCB specimens were prepared by first bonding loading blocks to the pre-delaminated end of the specimen. Subsequently, a white chalk coating was applied to the side surface to enhance

crack visibility. A series of reference markers was then applied along the specimen length to enable accurate monitoring of the delamination front position during testing. The first marker was placed 1 mm beyond the edge of the non-adhesive insert, corresponding to a distance of 47 mm from the specimen edge (the insert length being 46 mm). A total of 16 markers were applied at 1 mm intervals, followed by three additional markers spaced at 10 mm intervals (Figure 6). The position of the delamination front was recorded when it reached the midpoint between successive markers, allowing determination of the crack length for fracture toughness calculations.

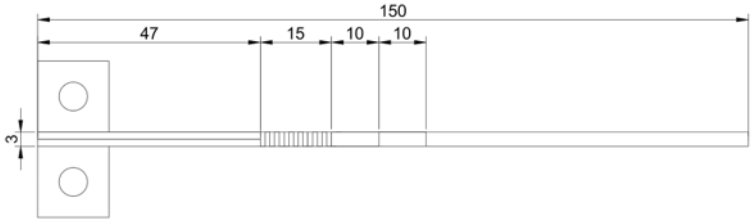

Fig. 6. Position of markers on DCB specimen

ENF

The ENF specimens were prepared by applying a white chalk coating to the specimen side surfaces to enhance crack visibility. The position of the non-adhesive insert edge was first marked. Subsequently, three reference markers were applied starting 20 mm from the insert edge, with a spacing of 10 mm (Figure 7).

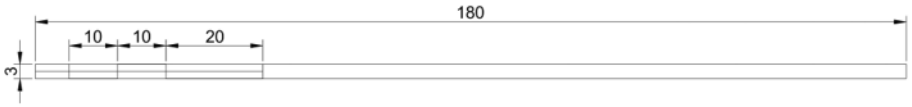

Fig. 7. ENF specimen with position of markers

MMB

The MMB specimens were prepared by first bonding the loading blocks to the specimen. The blocks were positioned in such a way that their midpoints were located 24 mm from the edge on the side of the non-adhesive insert. Subsequently, a white chalk coating was applied to the specimen's side surface to enhance crack visibility. A series of reference markers was then applied, starting 1 mm from the edge of the non-adhesive insert. Five markers were placed at 1 mm intervals, followed by two additional markers spaced at 10 mm intervals (Figure 8).

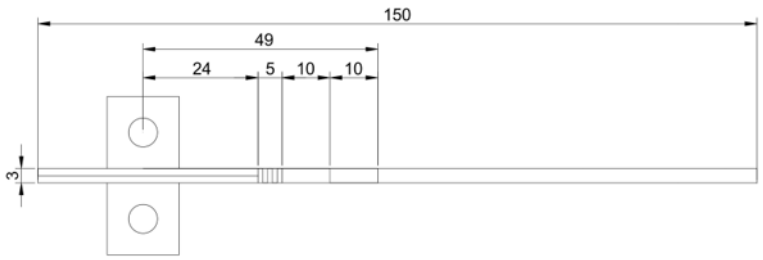

Fig. 8. MMB specimen with positions of markers

Experimental procedure

DCB

The DCB specimen is mounted in the testing machine using grips that allow the attachment of loading adapters. The adapters must be aligned within a single plane, which can be verified by checking for any lateral offset between their side surfaces. After correct alignment, the adapters are positioned as close as possible using the machine control system, allowing the specimen to be inserted between them. The holes in the bonded loading blocks must be coaxially aligned with the adapter holes, which may require minor adjustment to adapter spacing. Finally, steel pins are inserted through the aligned holes to secure the specimen. A properly assembled test configuration is shown in Figure 9.

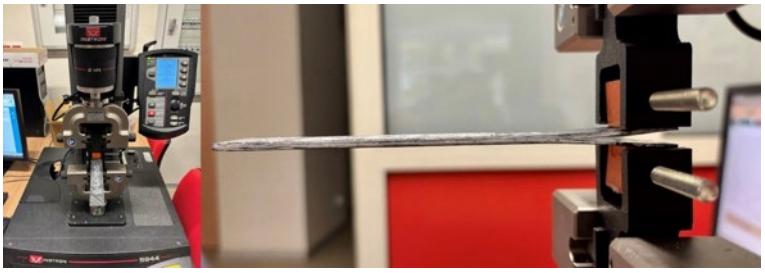

Fig. 9. DCB specimen mounted in testing setup

The test is conducted at a crosshead displacement rate between 1–5 mm/min. The initial crack opening is minimized to avoid influence on the results. During the test, crack propagation is monitored by means of an optical magnification system while the corresponding load and displacement values are recorded at each marked crack increment [31].

ENF

The specimen is positioned on a three-point bending fixture with a support span of L = 100 mm. The loading system consists of two lower supports and a single upper loading roller, all with rounded contact surfaces to avoid premature cutting or local damage of the specimen. The specimen is placed on the supports with the correct orientation, and the loading nose is positioned close to the surface [29]. The test setup is shown in Figure 10.

The test is performed at a crosshead displacement rate of 0.5 mm/min and consists of three loading stages. Each stage is used to determine specimen compliance as a function of crack length a, which varies with the loading position. The first two stages are conducted within the elastic regime to ensure linear response. Based on preliminary calibration, the load levels ensuring elastic deformation were determined as 50 N for a = 20 mm and 80 N for a = 40 mm.

In the first and second stages, compliance is measured at predefined crack lengths (a = 20 mm and a = 40 mm, respectively), followed by unloading to the initial configuration. The third stage is performed at a = 30 mm and loaded up to the maximum force corresponding to unstable crack growth, identified by a pronounced load drop. The obtained compliance values are used to determine exponent m, which is required for the evaluation of fracture energy [29].

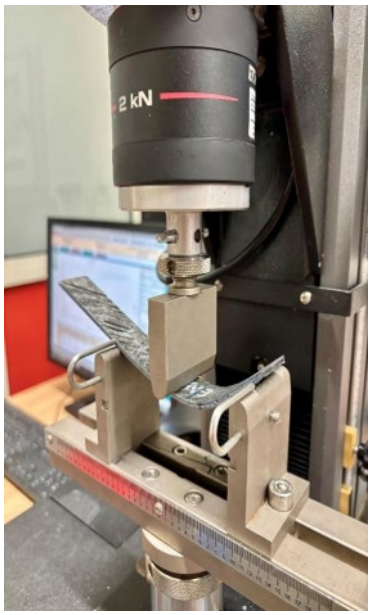

Fig. 10. ENF test setup with specimen during loading

 All rights reserved

MMB

The test is performed at a crosshead displacement rate of 0.5 mm/min. The specimen is mounted by bonding loading blocks to the side containing the non-adhesive insert, with their axis positioned at a distance of 24–30 mm from the end of the insert. Before testing, the critical geometric parameter defining the distance between the fixture rotation point and the load application point is set, as it governs the mode I/mode II load ratio.

The specimen is installed in a two-part loading fixture and secured using pins, after which the assembly is mounted in the testing machine (Figure 11). Before loading, the actuator is positioned at the initial position, and the force and displacement signals are zeroed. A slight preload is then applied to ensure proper contact between the loading nose and the specimen.

The mode mixity is controlled by the lever geometry of the fixture, where the relative distance between the reference points determines the proportion of Mode I and Mode II contributions during loading. In this work two mixities were tested: ϕ=33% and ϕ=48%.

During the experiment, crack propagation is monitored, and the onset of crack growth into the specimen is identified based on the force response and recorded as P_{VIS}. The test continues until the maximum energy value is reached and the crack front has propagated through all the predefined 1 mm increment markers.

Fracture energy is determined based on characteristic points identified from the load–displacement curve. Linear regression of the elastic region is first performed, and its intersection with the experimental curve defines the P_{NL} point, corresponding to the onset of non-linear behavior in the specimen. Next, a second line with a slope equal to 95% of the initial stiffness (0.95·m) is constructed. Its intersection with the load–displacement curve defines the $P_{5\%max}$ point. If the force at this point is lower than the maximum recorded force, the maximum force value is adopted instead. The fracture energy calculated using P_{VIS} represents the onset of visible crack propagation and usually provides conservative values. The P_{NL} criterion corresponds to the initiation of damage within the laminate, while the $P_{5\%max}$ criterion generally yields the highest and most repeatable fracture energy values.

Fig. 11. MMB test setup

Data analysis

The fracture toughness was evaluated for mode I (DCB), mode II (ENF), and mixed-mode (MMB) loading conditions employing beam theory-based approaches. Energy release rate G was calculated based on experimentally measured load–displacement data and crack length monitoring.

The fracture toughness was evaluated for mode I (DCB), mode II (ENF), and mixed-mode (MMB) loading conditions employing beam theory-based approaches. Energy release rate G was calculated based on experimentally measured load–displacement data and crack length monitoring.

Mode I – DCB

Mode I interlaminar fracture toughness G was determined by means of two data reduction methods: the modified beam theory (MBT) and the compliance calibration (CC) method. The use of both approaches allows cross-validation of the results and reduces the uncertainty associated with model assumptions

 All rights reserved

Modified beam theory

The modified beam theory (MBT) is based on classical beam theory with corrections accounting for non-ideal effects such as crack tip rotation and large displacements. In this approach, the energy release rate is calculated using an effective crack length ($a + |\Delta|$), where Δ is a correction term determined experimentally. Fracture energy G_{Ic} was calculated according to the MBT formulation (1), where P_c is the critical load, δ_c is the actuator displacement associated with the critical load value, b is the specimen width, while F and N are correction factors.

$$G_{Ic} = \frac{3 \cdot P_c \cdot \delta_c \cdot F}{2 \cdot b \cdot (a+|\Delta|) \cdot N} \left[\frac{J}{m^2}\right] \quad (1)$$

Factor F represents a correction for large displacements, while factor N accounts for both large displacement effects and the characteristics of the loading system. Parameters F and N are determined analytically (Eq. 2 and 3) and evaluated individually for each specimen.

$$N = 1 - \left(\frac{L'}{a}\right)^3 - \frac{9}{3} \cdot \left[1 - \left(\frac{L'}{a}\right)^2\right] \cdot \left(\frac{\delta_c \cdot t}{a^2}\right) - \frac{9}{35} \cdot \left(\frac{\delta_c}{a}\right)^2 \quad (2)$$

$$F = 1 - \frac{3}{10} \cdot \left(\frac{\delta_c}{a}\right)^2 - \frac{3}{2} \cdot \left(\frac{\delta_c \cdot t}{a^2}\right) \quad (3)$$

The Δ parameter is determined from the linear relationship between $(C/N)^{1/3}$ and delamination length a, and is calculated as ratio *-b/a* obtained from the equation of the fitted function.

Compliance calibration method

In contrast, the compliance calibration (CC) method is based on an empirical relationship between specimen compliance and crack length. The compliance is defined as (4), where δ represents the actuator displacement recorded when the crack front passes a measurement marker, while P denotes the corresponding load value.

$$C = \frac{\delta}{P} \left[\frac{mm}{N}\right] \quad (4)$$

Mode I fracture toughness G_{Ic} is calculated as (5), where m represents the slope of the function describing the relationship between log(*C/N*) and log(a). The remaining parameters are equivalent to those used in the MBT method description.

$$G_{Ic} = \frac{m \cdot P_c \cdot \delta_c \cdot F}{2 \cdot b \cdot a \cdot N} \left[\frac{J}{m^2}\right] \quad (5)$$

Mode II – ENF

Mode II interlaminar fracture toughness G_{II} was determined using the end-notched flexure (ENF) test configuration. The evaluation was based on beam theory, considering the specimen as a beam subjected to three-point bending. In this approach, the energy release rate is expressed as (6), where m represents the slope of the function describing the relationship between compliance (C) and crack length (a), P_{max} denotes the critical load corresponding to mode II crack propagation, a_0 is the distance between the insert end and the support in the ENF test configuration, and B represents the width of the tested specimen.

$$G_{IIc} = \frac{3 \cdot m \cdot {P_{max}}^2 \cdot {a_0}^2}{2 \cdot B} \left[\frac{J}{m^2}\right] \quad (6)$$

The compliance (C) was determined as the inverse of stiffness (E), where the stiffness corresponds to coefficient a (the slope of the curve) obtained from the load–displacement relationship).

Mixed mode I/II – MMB

The mixed-mode interlaminar fracture toughness was evaluated using the mixed-mode bending (MMB) test, which enables simultaneous loading in mode I and mode II. The method combines features of the DCB and ENF configurations, allowing controlled variation of the mode mixity through the loading geometry.

The total energy release rate is defined as (7), where the individual components correspond to mode I and mode II contributions, respectively.

$$G = G_I + G_{II} \left[\frac{J}{m^2}\right] \quad (7)$$

Mode I component G_I was determined using Equation 8, where P is the selected load value corresponding to the chosen initiation criterion, as described in Section 2.4.3., a is the distance between the insert end and the axis of the loading block hole, c is the distance between the rotation center of the upper loading fixture and the axis of the locking pin hole, and L is the distance between the support and the rotation center of the upper fixture. Parameter χ represents the crack length correction factor, h is half of the specimen thickness, b is the specimen width, and E_{1f} is the flexural modulus of elasticity. Similarly, mode II component G_{II} was calculated by means of Equation 9.

$$G_I = \frac{12 \cdot P^2 \cdot (3 \cdot c - L) \cdot (a + \chi \cdot h)^2}{16 \cdot b^2 \cdot h^3 \cdot L^2 \cdot E_{1f}} \left[\frac{J}{m^2}\right] \quad (8)$$

$$G_{II} = \frac{9 \cdot P^2 \cdot (c + L) \cdot (a + 0.42 \cdot \chi \cdot h)^2}{16 \cdot b^2 \cdot h^3 \cdot L^2 \cdot E_{1f}} \left[\frac{J}{m^2}\right] \quad (9)$$

Flexural modulus of elasticity E_{1f} was determined using Equation 10, where C is the compliance parameter.

$$E_{1f} = \frac{8 \cdot (a \cdot \chi \cdot h)^3 \cdot (3 \cdot c - L)^2 + \left[6 \cdot (a + \chi \cdot h)^3 + 4 \cdot L^3\right] \cdot (c + L)^2}{16 \cdot L^2 \cdot b \cdot h^3 \cdot C} \; [MPa] \quad (10)$$

The crack length correction factor was calculated with Equation 11, where the E_{11} is the longitudinal modulus of elasticity, G_{13} is the out-of-plane shear modulus, and Γ represents the transverse modulus correction parameter, determined based on Equation 12, where E_{22} is the transverse modulus of elasticity.

$$\chi = \sqrt{\frac{E_{11}}{11 * G_{13}} * \left[3 - 2 * \left(\frac{\Gamma}{1+\Gamma}\right)^2\right]} \quad (11)$$

$$\Gamma = 1.18 * \frac{\sqrt{E_{11} E_{22}}}{G_{13}} \quad (12)$$

RESULTS

Mode I – DCB

Figure 12 presents the variation of mode I fracture energy G_I as a function of crack length a, determined using both the CC and MBT methods for the tested DCB specimens (DCB-X series). Both methods exhibit a similar overall trend, characterized by a decrease in the energy release rate with increasing crack length, followed by a region of gradual stabilization. This behavior deviates from the classical rising R-curve typically observed in composite structures [32]. For ±45° filament-wound specimens, this response may be associated with the progressive loss of fiber bridging and increasing influence of matrix-dominated fracture mechanisms. The MBT and CC results are generally consistent, although slight differences can be observed between the two approaches. These discrepancies are attributed to the different assumptions underlying each method. The MBT method incorporates a correction of the effective crack length, while the CC method relies on experimentally fitted compliance data. Despite these differences, the agreement between the two methods confirms the reliability of the fracture toughness evaluation. Minor scatter in the results is observed. This variability may be associated with local material heterogeneities, such as resin-rich areas or voids.

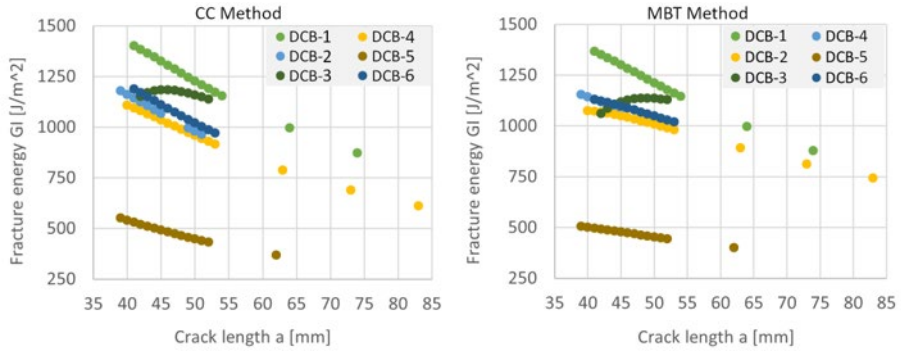

Fig. 12. Fracture toughness GI evolution as a function of crack length for all DCB test specimens determined by CC (left) and MBT methods (right)

The load–displacement curves for all the tested specimens are presented in Figure 13. The curves exhibit an initial linear region corresponding to elastic behavior, followed by gradual deviation from linearity associated with crack initiation and propagation. After reaching the maximum load, a reduction in stiffness is observed, indicating progressive delamination growth. In most cases, the load decreases gradually rather than abruptly, which suggests stable crack propagation during the test.

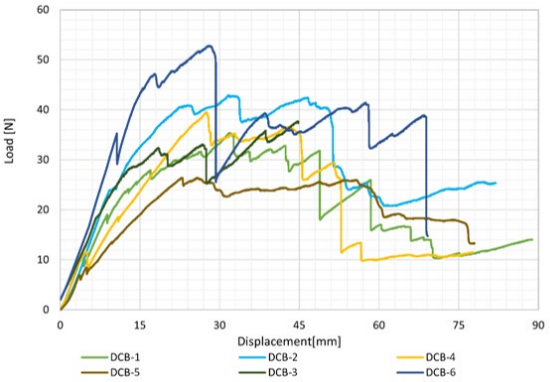

Fig. 13. Load–displacement curves for all DCB specimens

Differences between individual specimens can be observed in both the maximum load and the post-peak response. These variations reflect the influence of cross-over sections. However, the overall shape of the curves remains consistent across all the samples, confirming the repeatability of the experimental procedure.

The maximum load values obtained for each specimen, along with qualitative observations of the crack propagation, are summarized in Table 1.

Table 1. **Assessment of crack propagation behavior during DCB test**

Specimen ID	Maximum force [N]	Crack propagation observation
DCB-1	36.4	Crack front does not migrate between layers for the entire crack length.
DCB-2	43.4	Crack begins to migrate between layers immediately after insert end.
DCB-3	37.7	Crack front does not migrate between layers for the entire crack length.
DCB-4	40.0	Crack begins to migrate between layers immediately after insert end.
DCB-5	27.3	Crack migrates between layers after passing two markers beyond insert end.
DCB-6	52.1	Crack front does not migrate between layers for the entire crack length.

Figure 14 illustrates the crack front migration observed for specimen DCB-5. As can be seen from the right-hand side of the image, the crack path changes its position as the displacement increases. This indicates that the crack does not propagate along a single, well-defined interface but instead migrates between adjacent layers during loading [31, 33]. This behavior suggests local variations in interlaminar properties, which may lead to instability of the crack path and influence the fracture process.

Fig. 14. Crack front migration during test for specimen DCB-5

Figure 15 shows the fracture surface of specimen DCB-2 after separation along the delamination plane, with the upper and lower adherends presented as two distinct parts. The insert initiating the crack is clearly visible on the left-hand side, while the crack propagates toward the right. The fracture surface is divided into four characteristic regions (A–D) [34], marked directly in the figure. Figure 16 shows the corresponding load–displacement curve with marked regions A–D. Region A corresponds to the initial stage of crack propagation immediately after the insert and is associated with the highest load levels observed during the test. Region B represents a transition zone in which a noticeable change in fracture surface morphology occurs, corresponding to a drop in force on the force–displacement curve. In Region C, the fracture surface exhibits a more regular

 All rights reserved

and oriented pattern, indicating stabilized crack growth at a reduced load level. Region D corresponds to the final stage of crack propagation, where the fracture surface becomes more irregular, suggesting increased instability of the crack path. The colored areas visible on the fracture surfaces highlight differences in the material structure. The yellow and blue regions represent fibers wound at +α and −α orientations, while the green regions indicate voids, most likely caused by air trapped between layers, particularly in the crossover zones. These variations in fracture surface morphology correlate with the changes observed in the mechanical response, confirming that local structural features significantly influence crack propagation behavior.

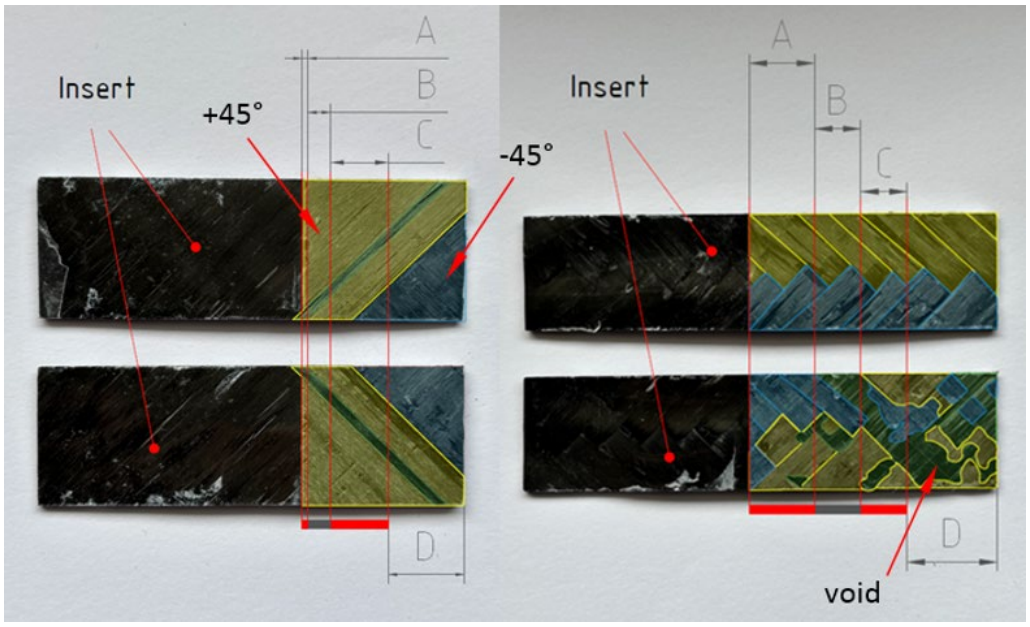

Fig. 15. Visual assessment of fracture surfaces of specimens DCB-1 (left) and DCB-5 (right)

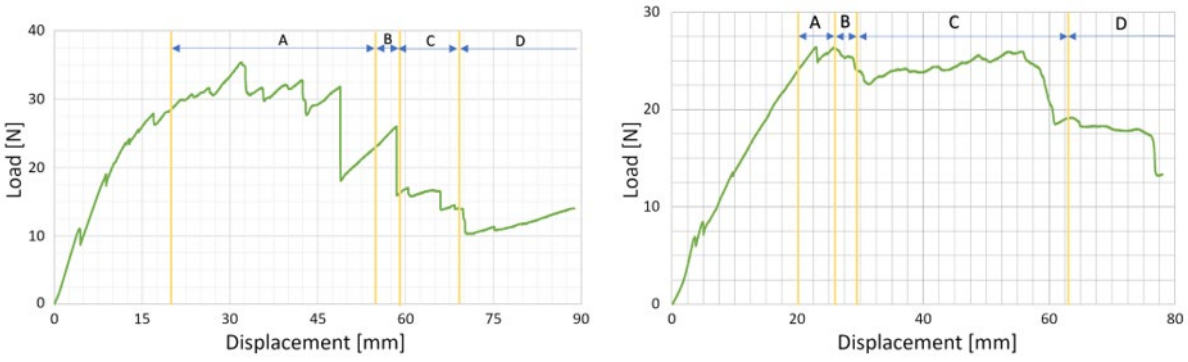

Fig. 16. Load–displacement curves corresponding to visual assessment of specimens DCB-1 (left) and DCB-1 (right)

ENF

Figure 17 presents the load–displacement curves obtained during the ENF tests for all the analyzed specimens. All the specimens exhibit a characteristic response typical for mode II interlaminar fracture testing. An initial linear region is observed at low displacement values, corresponding to elastic deformation of the specimen. With increasing displacement, the curves gradually transition into a nonlinear regime associated with crack initiation and propagation.

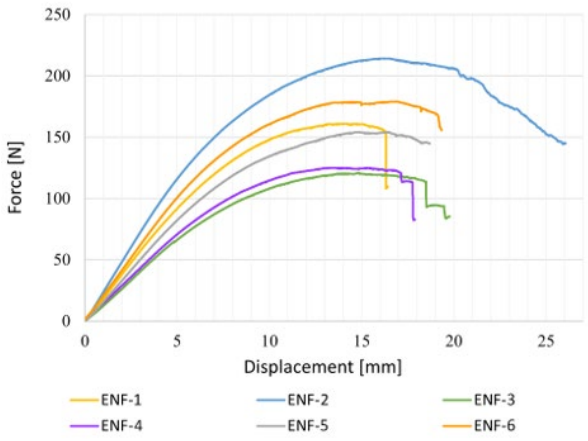

Fig. 17. Load–displacement curves for all ENF specimens

The highest load-carrying capacity was recorded for specimen ENF-2, which reached a maximum load exceeding 210 N. Lower maximum loads were observed for specimens 3 and 4, whose peak loads remained in the range of approximately 120 N.

Differences between the curves were also observed in the post-peak region. Specimen ENF-2 exhibited the smoothest and most gradual decrease in load after the maximum value, indicating relatively stable crack propagation and higher resistance to interlaminar shear fracture. In contrast, several specimens, particularly 1, 3, and 4, exhibited sudden load drops during propagation, which may indicate local instability of crack growth or the presence of structural heterogeneities within the laminate.

The calculated Mode II fracture toughness values G_{II} are presented in Figure 18. The highest fracture energy was obtained for specimen no. 1, followed by specimens 2, 4, 5, 6 and 3.

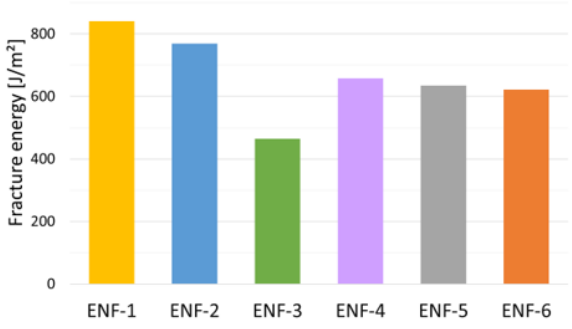

Fig. 18. Fracture energy GIIc for all ENF specimens

Although ENF-2 achieved the highest maximum load during the ENF test, ENF-1 exhibited the highest calculated fracture energy, indicating that the energy absorption capability during crack propagation was not directly proportional to the peak load value alone.

Overall, the ENF results demonstrated noticeable variability between the specimens, which may be associated with local differences in fiber arrangement, resin distribution, void content, or interfacial bonding quality. Nevertheless, all the tested specimens exhibited progressive crack propagation characteristic for laminated composite structures subjected to mode II interlaminar fracture loading.

MMB

Figure 19 presents the load-displacement curves obtained during MMB testing for all the analyzed specimens with two groups of mode mixity $\phi = 0.33$ (specimens 1, 2, 3) and $\phi = 0.48$ (specimens 4, 5, 6). All the specimens exhibited an initial linear region corresponding to their elastic response. In this stage, the load increased proportionally with displacement, indicating stable stiffness of the laminate before crack initiation.

After reaching the end of the elastic range, deviations from linearity were observed, associated with the initiation and progressive propagation of delamination. The specimens generally exhibited a gradual increase in load up to the maximum value, followed by a load drop related to crack growth and a reduction in structural stiffness. Specimen no. 5 reached the highest maximum load and displayed the steepest initial slope, different from the other $\phi = 0.48$ mode mixity specimens, indicating the highest stiffness and fracture resistance. The post-peak region was characterized by a gradual force reduction and multiple small load drops associated with progressive crack propagation.

For both mode mixity ratios, stable crack propagation behavior was observed in most of the specimens, although local sudden drops in force indicated unstable increments in delamination growth. The specimens tested at $\phi = 0.48$

generally exhibited higher maximum loads and steeper initial slopes, suggesting increased stiffness and higher resistance to crack propagation under a greater mode II contribution.

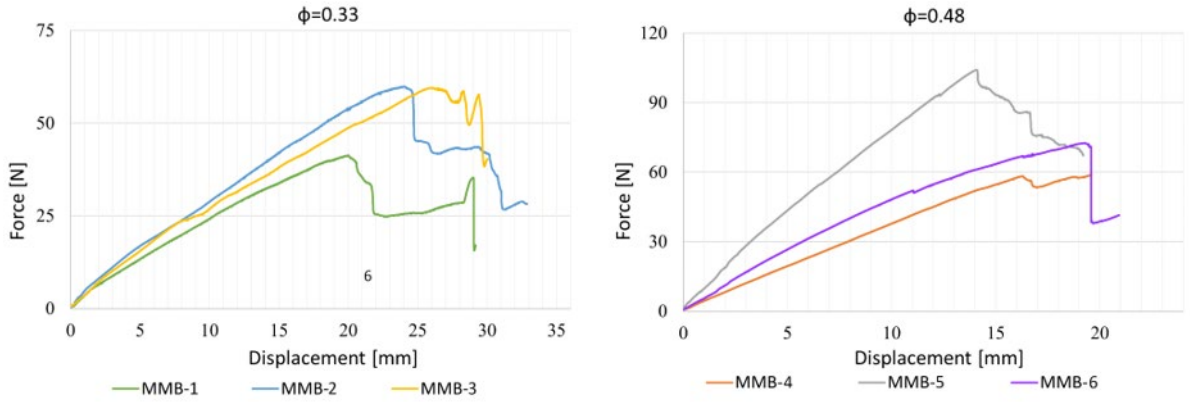

Fig. 19. Load-displacement curve for ϕ=0.33 mixity specimens (left), ϕ=0.48 mixity (right)

The curves obtained for ϕ = 0.33 demonstrated a more extended post-critical response and greater displacement prior to complete crack propagation. The fracture energy results obtained for both the mode mixity ratios exhibited noticeable scatter between individual specimens (Figure 20), which is typical for interlaminar fracture tests of composite laminates. Nonetheless, several general trends can be observed. For all the specimens, the fracture energy determined using the P_{VIS} and $P_{5\%max}$ criteria was higher than the values obtained by means of the P_{NL} method, reflecting the progressive accumulation of energy during crack propagation after the onset of nonlinearity.

The specimens tested at ϕ = 0.33 generally exhibited higher fracture energy values compared to those tested at ϕ = 0.48, indicating increased resistance to delamination growth with a greater contribution of mode I loading.

Among the evaluated methods, the $P_{5\%max}$ criterion typically resulted in the highest fracture energy values since it corresponds to a later stage of crack development and includes additional energy dissipation during stable crack propagation.

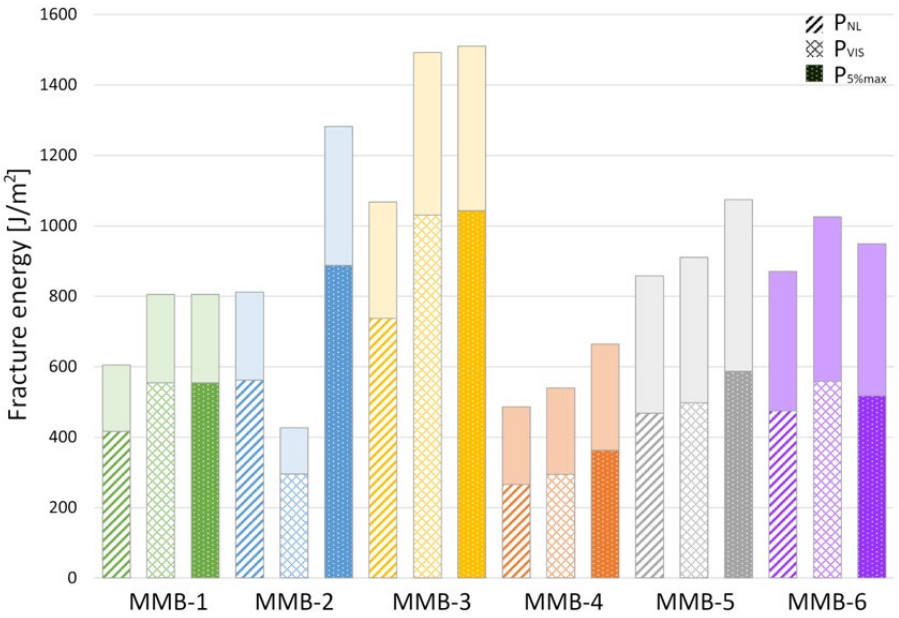

Fig. 20. PNL, PVIS, P5%max fracture energy for all MMB specimens

DISCUSSION

Effect of fiber orientation and fiber cross-over

The mode I fracture toughness values for most of the specimens during crack propagation were approximately 900-1400 J/m^2. The DCB test results for the multidirectional filament-wound specimens are generally similar to those reported in the literature for multidirectional carbon epoxy composite specimens and higher than for unidirectional specimens. Choi et al. [35] reported maximum G_{IC} values for multidirectional laminates ranging from 690 to 1290 J/m² and a value of 300 J/m² for a unidirectional laminate. The results obtained in the present study for filament-wound specimens are also similar to those reported for twill-woven composites [36]. For comparison, Ramkumar et al. [37] reported fracture energies of 102.6 J/m^2 for a unidirectional T300/5208 carbon/epoxy laminate and a very close value of 100.0 J/m^2 for a multidirectional laminate made from the same material, indicating that the off-axis plies alone do not lead to higher mode I fracture toughness. Similarly, values of approximately 205-262 J/m² have been reported for unidirectional IM7/8552 carbon/epoxy [38]. The higher values observed by most of the specimens in the present study may therefore be related to the specific wound fiber structure and the associated crack-propagation mechanisms rather than solely to the fiber orientation.

According to previous studies, mode I interlaminar fracture toughness G_I tends to grow with an increasing mismatch in fiber orientations between adjacent layers. This effect may be relevant in the present ±45° wound configuration, where strong ply-to-ply orientation differences can promote additional energy dissipation during crack propagation [33]. However, noticeable differences in fracture energy were observed between individual specimens. These variations were associated with the crack front migration phenomena described in Table 1 and observed in Figure 15. The migration of the crack front resulted from the angular arrangement of the fibers within the laminate structure, which altered the local crack propagation path during delamination growth.

Specimen DCB-1 exhibited a fracture energy value approximately 27% higher than the remaining specimens. At the same time, this specimen had a significantly greater number of fiber cross-over regions than the other tested samples, as shown in Figure 15. This observation suggests that an increased number of fiber interlacements may enhance the resistance to crack propagation in the composite structure. The cross-over regions likely acted as local obstacles to delamination growth, forcing the crack front to deviate from its original path and increasing the energy required for further propagation. Analysis of the load–displacement curves presented in Figure 16 additionally indicated that the specimen with the larger number of fiber cross-overs exhibited less stable propagation behavior compared to the specimen containing fewer interlaced regions. The sudden load drops visible in the load–displacement response can be attributed to repeated crack front interactions with the fiber cross-over zones. These local structural heterogeneities temporarily raised the crack propagation resistance, followed by abrupt crack advancement after overcoming the reinforced regions.

The mode II ENF fracture toughness values obtained in the present study were comparable with those reported in the literature for unidirectional laminates [36]. Nevertheless, they were approximately two times lower than the values reported for twill-woven composite structures. This behavior suggests that, unlike in the DCB tests, the helical fiber arrangement did not enhance the resistance to shear-driven delamination. Twill architectures provide a larger number of fiber interlacements, which can act as effective barriers to crack propagation under mode II loading. In the present filament-wound laminates, although the angular fiber orientation influenced the crack path, the density of the fiber cross-over regions appears to be insufficient to achieve the level of crack-bridging and energy dissipation observed in woven composites. As a result, the mode II fracture toughness remained comparable to unidirectional laminates while remaining lower than that of twill-reinforced structures.

 All rights reserved

Effect of voids

The presence of voids in the manufactured composite material may also have had a significant influence on its mechanical performance and fracture resistance. By analyzing regions A, B, C and D presented in Figure 15 and comparing them with the corresponding sections of the load–displacement curve shown in Figure 16, a distinct decrease in load can be observed within regions B and C. These areas correspond to locations containing a considerable number of voids within the matrix material. The presence of voids may have locally weakened the laminate structure and reduced the efficiency of stress transfer between the fibers and the matrix, which resulted in lower resistance to crack propagation. In contrast, region D exhibited a slight increment in load, which can be associated with a reduced concentration of voids in that area. This observation indicates that a decreasing void content improves the local fracture resistance of the composite material.

Overall, the results suggest that an increasing void content negatively affects the fracture toughness of the laminate by facilitating crack growth and reducing structural integrity. At the same time, the fracture behavior may also be influenced by the complex fiber structure and the presence of fiber cross-over regions, indicating the coexistence of multiple interacting mechanisms affecting crack propagation.

Effect of mode mixity

The MMB tests were performed for two different mode mixity ratios corresponding to mode I contributions of 33% and 48% to the total fracture energy. Analysis of the results presented in Figure 20 reveals that higher fracture energy values were obtained for the 33% mode mixity ratio. This indicates that the fracture resistance of the composite material grew with an increasing contribution of the mode I component (G_{IC}) to the total mixed-mode fracture energy (G_c) under combined loading conditions.

Comparison of the load–displacement curves (Figure 19) and fracture energy values presented in Figure 20 shows that the energies determined using the P_{VIS} and P_{NL} criteria were very similar. This suggests that crack propagation occurred in a relatively stable and uniform manner throughout the specimens. The initiation of internal crack growth and crack propagation observed at the specimen edges occurred simultaneously, indicating consistent delamination development across the laminate thickness.

For the specimens tested at the mode mixity ratio of $\phi = 33\%$, the measured fracture energy values were approximately twice as high as those reported in [36]. In contrast, for $\phi = 48\%$, the obtained values were comparable to previously published results. The literature data generally concern laminates with straight, unidirectional fiber arrangements or twill laminates. Comparison with the present results suggests that the angular fiber orientation used in the analyzed specimens significantly raised the fracture resistance at lower mode mixity ratios.

This behavior can be attributed to the influence of the angled fiber architecture on the crack propagation mechanisms. Fibers arranged at an angle hinder crack opening and force the crack front to propagate along a more complex path within the laminate structure. As a result, additional energy is required for delamination growth, leading to increased fracture toughness under mixed-mode loading conditions.

CONCLUSIONS

- The Mode I fracture energy of helically wound laminates exceeded several literature values reported for unidirectional carbon/epoxy composites, although no direct comparison was performed.
- The presence of voids in the composite structure negatively affects fracture toughness and promotes unstable crack growth.
- Fiber interlacing improves toughness in the DCB test but reduces the stability of crack propagation.
- Increasing the mode I contribution in the MMB test enhances the overall fracture resistance.
- Fiber orientation plays a role in determining the fracture behavior under mixed-mode loading.

 All rights reserved

Author contributions

Conceptualization, P.S. and W.B..; methodology, P.S.; validation, J.S. and M. Bogucki; formal analysis, Z.P., K.P., J.S. and M. Bogucki; investigation, J.S. and M. Bogucki; resources, P.B. and K.T.; data curation, J.S.; writing–original draft preparation, Z.P. and K.P.; writing–review and editing, Z.P., K.P. and M. Barcikowski; visualization, M. Barcikowski and W.B.; supervision, P.S.; project administration, P.S.; funding acquisition, P.S. All authors have read and agreed to the published version of the manuscript.

Funding

This research was funded by the National Science Centre Poland (NCN) [Narodowe Centrum Nauki] under the MINIATURA 8 program, grant number 2024/08/X/ST8/01480".

Data availability statement

The original contributions presented in this study are included in the article. Further inquiries can be directed to the corresponding author.

Conflicts of interest

The authors declare no conflicts of interest.

Abbreviations

The following abbreviations are used in this manuscript:

FRP	Fiber-reinforced polymer
DCB	Double cantilever beam
ENF	End-notched flexure
MMB	Mixed-mode bending
MBT	Modified beam theory
CC	Compliance calibration

REFERENCES

[1] Nurazzi, N.M., Asyraf, M.R.M., Fatimah Athiyah, S., Shazleen, S.S., Rafiqah, S.A., Harussani, M.M., Kamarudin, S.H., Razman, M.R., Rahmah, M., Zainudin, E.S., Ilyas, R.A., Aisyah, H.A., Norrrahim, M.N.F., Abdullah, N., Sapuan, S.M., & Khalina, A. A review on mechanical performance of hybrid natural fiber polymer composites for structural applications. Polymers 2021, 13(13). https://doi.org/10.3390/polym13132170

[2] Bouhamed, A., chaari, R., Aloulou, J., Attaoui, A., Scholze, M., Wöpke, C., Richter, P., Dehnert, M., Khlif, M., Tegenkamp, C., Wagner, M.F.X., & Kanoun, O. Sustainable high-performance natural fiber composites with integrated strain sensing for aeronautics and automotive applications. Surfaces and Interfaces 2025, 75, 107740. https://doi.org/10.1016/J.SURFIN.2025.107740

[3] Gupta, M.K., Singhal, V., & Rajput, N.S. Applications and Challenges of Carbon-fibres reinforced Composites: A Review. Evergreen 2022, 9(3), 682–693. https://doi.org/10.5109/4843099

[4] Fowler, C.P., Orifici, A.C., & Wang, C.H. A review of toroidal composite pressure vessel optimisation and damage tolerant design for high pressure gaseous fuel storage. International Journal of Hydrogen Energy 2016, 41(47), 22067–22089. https://doi.org/10.1016/j.ijhydene.2016.10.039

[5] Vasiliev, V.V., Krikanov, A.A., & Razin, A.F. New generation of filament-wound composite pressure vessels for commercial applications. Composite Structures 2003, 62(3–4), 449–459. https://doi.org/10.1016/j.compstruct.2003.09.019

[6] [6] Fang, P., Xu, Y., Yuan, S., Bai, Y., & Cheng, P. Investigation on mechanical properties of fibreglass reinforced flexible pipes under torsion. Proceedings of the International Conference on Offshore Mechanics and Arctic Engineering – OMAE, 2018 7B(June). https://doi.org/10.1115/OMAE2018-77354

[7] Schmidt F., Walter M., Richter J., Geller S., Gude M., Optimisation of wet winding process parameters for the production of type IV hydrogen pressure vessels with high gravimetric storage density, Composites Theory and Practice 2025 September, 25, 3, 157–165, https://doi.org/10.62753/ctp.2025.02.3.3

[8] [8] Bisheh, H. Design and analysis of hybrid natural/synthetic fibre-reinforced composite automotive drive shafts. Structures 2024, 61, 106057. https://doi.org/10.1016/J.ISTRUC.2024.106057

[9] Nawawithan, N., Kittisakpairach, P., Nithiboonyapun, S., Ruangjirakit, K., & Jongpradist, P. Design and performance simulation of hybrid hemp/glass fiber composites for automotive front bumper beams. Composite Structures 2024, 335, 118003. https://doi.org/10.1016/J.COMPSTRUCT.2024.118003

[10] Czerwinski, F. Current Trends in Automotive Lightweighting Strategies and Materials. Materials 2021, 14(21), 6631. https://doi.org/10.3390/MA14216631

[11] Shyamsunder, L., Maurya, A., Rajan, S.D., Cordasco, D., Revilock, D., & Blankenhorn, G. Impact simulation of composite panels for aerospace applications. Composites Part B: Engineering 2022, 247, 110320. https://doi.org/10.1016/J.COMPOSITESB.2022.110320

[12] [12] Xu, J., Wang, L., Liu, M., Tian, J., Liu, B., & Liu, X. Patterns design of filament wound spherical structure based on a new winding strategy. Journal of Reinforced Plastics and Composites 2019, 38(7), 314–322. https://doi.org/10.1177/0731684418817147

[13] Duda, S., Smolnicki, M., Stabla, P., Zielonka, P., Osiecki, T., Gao, C., & Lesiuk, G. Experimental characterization and modeling of cylindrical CFRP structures under quasi-static multiaxial loading conditions. Thin-Walled Structures 2024, 195(July 2023). https://doi.org/10.1016/j.tws.2023.111364

 All rights reserved

[14] Hamed, A.F., Khalid, Y.A., Sapuan, S.M., Hamdan, M.M., Younis, T.S., & Sahari, B.B. Effects of winding angles on the strength of filament wound composite tubes subjected to different loading modes. Polymers and Polymer Composites 2007, 15(3), 199–206. https://doi.org/10.1177/096739110701500304

[15] Ueda, M., Hidaka, T., Ichihara, N., Yang, H., Iwase, W., Matsuda, T., Morita, N., Aoki, R., & Yokozeki, T. Voids in type-IV composite pressure vessels manufactured by a dry filament-winding process. International Journal of Pressure Vessels and Piping 2024, 208, 105154. https://doi.org/10.1016/J.IJPVP.2024.105154

[16] Popiela, B., Kim, K., Lee, K. J., & Lee, J. R. Impact of internal pressure regulation in filament winding on the quality of composite cylinders: a study with pulse-echo ultrasonic propagation imaging. Advanced Composite Materials 2025. https://doi.org/10.1080/09243046.2025.2547457

[17] Almeida, J.H.S., St-Pierre, L., Wang, Z., Ribeiro, M.L., Tita, V., Amico, S.C., & Castro, S.G.P. Design, modeling, optimization, manufacturing and testing of variable-angle filament-wound cylinders. Composites Part B: Engineering 2021, 225, 109224. https://doi.org/10.1016/J.COMPOSITESB.2021.109224

[18] Gong, Y., Zhao, L., Zhang, J., Wang, Y., & Hu, N. Delamination propagation criterion including the effect of fiber bridging for mixed-mode I/II delamination in CFRP multidirectional laminates. Composites Science and Technology 2017, 151, 302–309. https://doi.org/10.1016/j.compscitech.2017.09.002

[19] Peng, L., Xu, J., Zhang, J., & Zhao, L. Mixed mode delamination growth of multidirectional composite laminates under fatigue loading. Engineering Fracture Mechanics 2012, 96, 676–686. https://doi.org/10.1016/j.engfracmech.2012.09.033

[20] Davidson, B.D., Krüger, R., & König, M. Three-dimensional analysis of center-delaminated unidirectional and multidirectional single-leg bending specimens. Composites Science and Technology 1995, 54(4), 385–394. https://doi.org/10.1016/0266-3538(95)00069-0

[21] Zhao, L., Wang, Y., Zhang, J., Gong, Y., Lu, Z., Hu, N., & Xu, J. An interface-dependent model of plateau fracture toughness in multidirectional CFRP laminates under mode I loading. Composites Part B: Engineering 2017, 131, 196–208. https://doi.org/10.1016/j.compositesb.2017.07.077

[22] Test Method for Mode I Interlaminar Fracture Toughness of Unidirectional Fiber-Reinforced Polymer Matrix Composites. ASTM International 2021. https://doi.org/10.1520/D5528_D5528M-21

[23] De Morais, A. B. Double cantilever beam testing of multidirectional laminates. Composites Part A: Applied Science and Manufacturing 2003, 34(12), 1135–1142. https://doi.org/10.1016/J.COMPOSITESA.2003.08.008

[24] Zhao, L., Gong, Y., Zhang, J., Wang, Y., Lu, Z., Peng, L., & Hu, N. A novel interpretation of fatigue delamination growth behavior in CFRP multidirectional laminates. Composites Science and Technology 2016, 133, 79–88. https://doi.org/10.1016/j.compscitech.2016.07.016

[25] Wilk, J. Compliance based method for testing fatigue delamination propagation in laminates. Engineering Fracture Mechanics 2018, 203, 137–151. https://doi.org/10.1016/j.engfracmech.2018.06.043

[26] Vallmajó, O., Descamps, M., Arteiro, A., & Turon, A. Effect of ply misalignment on the notched strength of composite laminates. Composite Structures 2025, 351. https://doi.org/10.1016/j.compstruct.2024.118589

[27] Pereira, A.B., de Morais, A.B., Marques, A.T., & de Castro, P.T. Mode II interlaminar fracture of carbon/epoxy multidirectional laminates. Composites Science and Technology 2004, 64(10–11), 1653–1659. https://doi.org/10.1016/J.COMPSCITECH.2003.12.001

[28] Gong, Y., Zhang, B., Mukhopadhyay, S., & Hallett, S.R. Experimental study on delamination migration in multidirectional laminates under mode II static and fatigue loading, with comparison to mode I. Composite Structures 2018, 201, 683–698. https://doi.org/10.1016/j.compstruct.2018.06.081

[29] Test Method for Determination of the Mode II Interlaminar Fracture Toughness of Unidirectional Fiber-Reinforced Polymer Matrix Composites. ASTM International 2019. https://doi.org/10.1520/D7905_D7905M-19E01

[30] Test Method for Mixed Mode I-Mode II Interlaminar Fracture Toughness of Unidirectional Fiber Reinforced Polymer Matrix Composites. ASTM International 2022. https://doi.org/10.1520/D6671_D6671M-22

[31] Gong, Y., Zhang, B., & Hallett, S. R. Delamination migration in multidirectional composite laminates under mode I quasi-static and fatigue loading. Composite Structures 2018, 189, 160–176. https://doi.org/10.1016/j.compstruct.2018.01.074

[32] Gfrerrer, M., Koss, V., Wiener, J., Schuecker, C., Brunner, A. J., & Pinter, G. Comparing Mode I, Mode II and Mixed-Mode I/II interlaminar fracture toughness of glass and carbon fiber reinforced polymer laminates with the same epoxy matrix system. Engineering Fracture Mechanics 2025, 320, 111009. https://doi.org/10.1016/J.ENGFRACMECH.2025.111009

[33] Perillo, G., & Echtermeyer, A. T. Mode I Fracture Toughness Testing of Composite Pipes. Applied Composite Materials 2013 20:6, 20(6), 1135–1146. https://doi.org/10.1007/S10443-013-9318-7

[34] Blondeau, C., Pappas, G., & Botsis, J. Influence of ply-angle on fracture in antisymmetric interfaces of CFRP laminates. Composite Structures 2019, 216, 464–476. https://doi.org/10.1016/J.COMPSTRUCT.2019.03.004

[35] Choi, N. S., Kinloch, A. J., & Williams, J. G. Delamination fracture of multidirectional carbon-fiber/epoxy composites under Mode I, Mode II and mixed-mode I/II loading. Journal of Composite Materials 1999, 33(1), 73–100. https://doi.org/10.1177/002199839903300105

[36] Banks-Sills, L., Shor, O., Simon, I., Chocron, T., & Fourman, V. Quasi-static modes I, II and mixed modes I/II fracture toughness of two laminate composites: Part I – Testing. Engineering Fracture Mechanics 2023, 277, 108934. https://doi.org/10.1016/J.ENGFRACMECH.2022.108934

[37] Ramkumar, R. L., & Whitcomb, J. D. Characterization of Mode I and Mixed-Mode Delamination Growth in T300/5208 Graphite/Epoxy. Delamination and Debonding of Materials, ASTM STP 876 1985, 315–335. https://doi.org/10.1520/STP36312S

[38] Czabaj, M. W., & Ratcliffe, J. G. Comparison of intralaminar and interlaminar mode I fracture toughnesses of a unidirectional IM7/8552 carbon/epoxy composite. Composites Science and Technology 2013, 89, 15–23. https://doi.org/10.1016/j.compscitech.2013.09.008